Journal of ELECTRONIC MATERIALS, Vol. 45, No. 7, 2016
DOI: 10.1007/s11664-016-4541-2
© 2016 The Minerals, Metals & Materials Society

CrossMark

Miniaturization of Micro-Solder Bumps and Effect of IMC on Stress Distribution

SOUD FARHAN CHOUDHURY[1,2] and LEILA LADANI[1,3]

1.—Department of Mechanical Engineering, University of Connecticut, Storrs, CT 06269-3139, USA. 2.—e-mail: soud.choudhury@uconn.edu. 3.—e-mail: lladani@engr.uconn.edu

As the joints become smaller in more advanced packages and devices, intermetallic (IMCs) volume ratio increases, which significantly impacts the overall mechanical behavior of joints. The existence of only a few grains of Sn (Tin) and IMC materials results in anisotropic elastic and plastic behavior which is not detectable using conventional finite element (FE) simulation with average properties for polycrystalline material. In this study, crystal plasticity finite element (CPFE) simulation is used to model the whole joint including copper, Sn solder and Cu_6Sn_5 IMC material. Experimental lap-shear test results for solder joints from the literature were used to validate the models. A comparative analysis between traditional FE, CPFE and experiments was conducted. The CPFE model was able to correlate the experiments more closely compared to traditional FE analysis because of its ability to capture micro-mechanical anisotropic behavior. Further analysis was conducted to evaluate the effect of IMC thickness on stress distribution in micro-bumps using a systematic numerical experiment with IMC thickness ranging from 0% to 80%. The analysis was conducted on micro-bumps with single crystal Sn and bicrystal Sn. The overall stress distribution and shear deformation changes as the IMC thickness increases. The model with higher IMC thickness shows a stiffer shear response, and provides a higher shear yield strength.

Key words: Cu_6Sn_5, solder joint, crystal plasticity finite element modeling, shear test, FE analysis, IMC

INTRODUCTION

The volume ratio of solder to copper in micro-solder bumps is very small compared to Ball grid array (BGA) solder balls and conventional solder joints. This implies that micro-solder bumps contain a small volume fraction of solder alloy with ample Cu supply which could result in the formation of thick IMC layers. IMC materials such as Cu_6Sn_5 and Cu_3Sn form inbetween the solder and Cu interface due to the diffusion of Cu into bulk Sn. In Cu pillar micro-bumps, a major portion of bulk solder transforms into IMCs during the diffusion process, and therefore the bump is usually left with a small volume fraction of ductile solder alloy.[1,2] A thin layer of IMCs is necessary for good metallurgical bonding;[3] however, thicker IMCs may have a negative effect on the mechanical performance of solder joints.[4–6] Complete transformation of bulk solder to IMCs has also been observed in recent studies.[2,7] IMC growth during reflow and isothermal aging have been studied by several researchers. IMC thickness increases with the increase in reflow time and temperature [2,8–10] and aging time and temperature.[11–13] IMC thickness is also largely affected by the cooling rate where it was observed that furnace cooling provides a larger IMC thickness than water quenching.[14] The effect of IMC thickness on the mechanical behavior of the solder joints have been explored in some studies.[8,9,15–23] Liu et al.[9] investigated the effect of different IMC thicknesses that were achieved during multiple reflows on the shear performance of solder joints. IMC growth and

(Received September 8, 2015; accepted April 12, 2016; published online April 28, 2016)

thickness were found to have insignificant effects on shear strength of SnAgCu solder joints. However, Bhat et al.[21] found an increase in shear strength of a SAC387/Cu joint with the increase in reflow temperature which was attributed to the increase in thickness of the Cu_6Sn_5 and Ag_3Sn IMC phases at higher reflow temperatures. In contrast, Deng et al.[17] observed a decrease in shear strength with the increase in IMC thickness after reflow and thermal aging processes. However, the decrease in shear strength during thermal aging was attributed to solder microstructure coarsening. The failure surface showed ductile fracture in all test cases which suggested that the failure was occurring at the bulk solder region, and that the shear strength was not sensitive to the thickness and morphology of IMCs. Lee et al.[20] also investigated the effect of solder microstructure coarsening, Ni addition, and IMC growth during reflow, and the thermal aging process on shear behavior. They observed a decrease in shear strength with the increase in reflow and thermal aging time.

However, all these analysis were conducted on solder joints with a thickness range of 0.20–2 mm[9,17,20] and the joint had a lower volume fraction of IMCs. Recently, a study conducted by Chen et al.[18] showed a major influence of IMC presence and thickness on shear strength. They conducted a single ball shear test on thermally aged micro-scale solder bumps with about 35 μm thickness that had a range of different IMC thicknesses due to different aging times. Shear strength decreased with the increase in IMC thickness. They also observed the failure mode transforming from ductile mode to the quasi-brittle mode with increasing aging times.

Joint thickness also showed a major impact on the shear strength and failure mode of the solder joint.[19,24] It was found that decreasing joint thickness results in a decrease in shear strength.[19] This trend was associated with the presence of Cu_6Sn_5 precipitates in the thicker joint, which were absent in the thinner joints.[19] Some limited studies have used modeling to evaluate the impact of IMC thickness on the mechanical behavior of solder joints.[17,25] However, due to differences in intrinsic material behavior from the bulk material behavior, these models are not able to successfully predict the actual behavior of small-scale joints.

It is very frequently observed that small joints and micro-bumps consist of IMCs with only a small numbers of grains, along with bulk Sn phase in single crystal, bicrystal or tricrystal modes.[26,27] This small number of grains introduces a strong anisotropic effect. Anisotropy is an important phenomena in all metals; however, it is unusually strong for Sn due to its body-centered tetragonal structure.[28,29] Subsequently, microstructural features such as grain numbers and grain orientation have significant effects on the mechanical properties and reliability of solder joints. Moreover, Cu_6Sn_5, which is the most common IMC material, shows anisotropic behavior due to its hexagonal crystal structure.[30]

Conventional finite element (FE) modeling is not capable of showing the actual micro-solder joint behavior. Matin et al.[31] examined the correlation between microscopic damage evolution and thermally induced stresses in a mechanically unconstrained solder alloy using a real microstructure. They combined optical imaging microscopy (OIM) with FE modeling using a simple linear elastic constitutive relationship. From the combination of OIM and FE modeling, they concluded that fatigue damage and stress induced by the thermal anisotropy of Sn is highly correlated. Park et al.[32] investigated the anisotropic behavior of solder joints using three-dimensional FE simulation using a linear elastic anisotropic model. They utilized a real microstructure, and studied the strain distribution in solder balls. Although both studies were useful in facilitating our understanding of the joints' behavior, they did not include plastic deformation which is the major contributor to damage and failure of these joints.

The CPFE method takes the effect of anisotropy and slip system behavior into consideration in modeling materials. There are few studies using the CPFE analysis method to understand the mechanical behavior of lead-free solder joints. Gong et al.[33] used a crystal viscoplasticity model to simulate the response of solder joints under thermal cyclic loading. They performed analyses with single crystal, bicrystal, and multicrystal morphologies. However, the morphologies and material properties were not realistic as they utilized bulk solder material properties, and also did not consider IMCs in the joint. Darbandi et al.[34] used a crystal plasticity model to investigate the effect of grain orientation on the activity of slip systems. Recently, the same group has published results on a CPFE study of deformation behavior of lead-free solder balls during shear loading.[35] The study shows the ability of CPFE analysis to predict the heterogonous deformation behavior of solder balls due to elastic and plastic anisotropy. In recent years, Maleki et al.[36] investigated the effect of aging condition on deformation behavior of SnAgCu solder with accurate geometry of Sn grains and IMCs by utilizing a J2 plasticity constitutive model. However, the model has isotropic plasticity which is unrealistic and oversimplified. There are a good number of published studies which have used the CPFE method to model the anisotropic behavior of solder joints; however, none of them considered the effect of IMCs. It is necessary to study the effect of slip deformation of substrate, solder, and IMCs in the same model to portray the actual behavior of the solder interconnect.

In this study, we present a CPFE model which is used to simulate the shear deformation mechanism and anisotropy associated with bulk solder, IMCs,

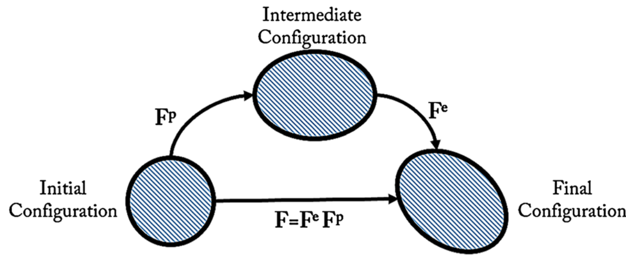

Fig. 1. Elastic–plastic deformation expressed using multiplicative decomposition of the deformation gradient.[42]

and a copper substrate. The study was conducted on single crystal and bicrystal solder alloys, and the effect of IMCs on the shear behavior of the overall solder joint was studied. A shear experiment was utilized from the literature to validate the accuracy of the model.

CRYSTAL PLASTICITY FINITE ELEMENT (CPFE) METHOD

Single crystal plasticity theory[37] assumes that plastic deformation is the sum of the crystalline slip in all activated slip systems. Plastic slip in a slip plane occurs when the resolved shear stress onto a crystallographic plane in the direction of slip reaches a critical value.[38] Rice and Hill[39] and Rice[40] formulated the precise theory to understand the plastic behavior of single and polycrystalline alloys. In this model, crystal deformation results from a combination of the elastic stretching and rotation of the lattice and plastic slip on the different slip systems. The essential constitutive relationships are briefly described in the following sections. A more detailed explanation is given in Huang et al.[41]

Total deformation gradient can be expressed using the multiplicative decomposition of the deformation gradient into elastic and plastic parts[42] (Fig. 1). Three configurations have been proposed to explain the deformation process. The elastic deformation is the reversible response of the lattice due to the external loads and displacements, and plastic deformation is an irreversible permanent deformation. According to the multiplicative decomposition method, first there is a plastic flow of material, starting at zero stress, from the initial configuration to the intermediate configuration, where lattice orientation and spacing are same as the reference configuration, followed by elastic deformation which contains stretching and rotation of the lattice.[42]

Lee's decomposition law[42] provides a sound kinematic and kinetic basis for elastoplastic constitutive analysis of single crystals. The total deformation gradient, $\mathbf{F}$, can be described by the following expression:

$$F = F^e F^p \tag{1}$$

Here, $\mathbf{F^e}$ = elastic deformation gradient which includes stretching and rotation, and $\mathbf{F^p}$ = plastic deformation gradient that includes crystallographic slip on the slip systems, where det$\mathbf{F^e} > 0$ and with incompressibility constraint det$\mathbf{F^P}$ = 1.

The stress–strain relationship is used in terms of the 2nd Piola-Kirchhof stress tensor ($\mathbf{S}$ = det $\mathbf{F^e F^{e-1} \sigma F^{e-T}}$) and the Lagrange Green strain tensor ($\mathbf{E^c}$ = (1/2) $\{\mathbf{F^{eT} F^e - I}\}$) such as:

$$S_{ij} = C_{ijkl} E^e_{kl} \tag{2}$$

where $\boldsymbol{C_{ijkl}}$ is the component of the elastic stiffness tensor when a material is oriented along its undeformed configuration, and can fully describe the anisotropic elastic behavior of a material. The plastic deformation gradient rate is stated in terms of the plastic velocity gradient and can be presented by:

$$\dot{\mathrm{F}}^{P} = L^p F^p \tag{3}$$

It is assumed during shearing that the plastic deformation occurs only due to the crystalline slip. Therefore, in a $\alpha = (\alpha_1 - \alpha_n)$ slip system, the plastic velocity gradient can be described as:

$$L^p = \sum_{\alpha_1}^{\alpha_n} \dot{\gamma}^\alpha \boldsymbol{s^\alpha} \tag{4}$$

where $\boldsymbol{s^\alpha}$ is the schmid tensor, which can be described as, $\boldsymbol{s^\alpha} = \boldsymbol{s^\alpha_i} \otimes \boldsymbol{m^\alpha_j}$. Here, $\boldsymbol{s^\alpha_i}$ and $\boldsymbol{m^\alpha_j}$ is slip direction and slip plane normal in the reference configuration and α_i is a specific slip system. $\otimes$ indicates the dyadic product of two tensors or vectors.

The plastic shearing rate or slipping rate, $\dot{\gamma}^\alpha$ in a rate-dependent crystalline solid can be expressed with the help of the viscoplastic flow rule. The flow rule gives the advantage of not using an iterative procedure to identify active slip systems. $\dot{\gamma}^\alpha$ can be presented in terms of corresponding resolved shear stress, τ^α[43] as:

$$\dot{\gamma}^\alpha = \tilde{\gamma} \left| \frac{\tau^\alpha}{\tau^o} \right|^{\frac{1}{m}} sgn(\tau^\alpha) \tag{5}$$

where $\tilde{\gamma}$ is the reference shearing rate, $\tau^\alpha = \alpha$th slip system critical resolved shear stress, $\tau^o = \alpha$th slip system initial critical resolved shear stress and m = strain rate sensitivity exponent. $\tilde{\gamma}$, and m are material properties. The impact of any set of slip systems, β, on the hardening behavior of a fixed slip system, α, can be expressed as slip system resistance or strain hardening through an incremental relationship, which can be expressed by the following relationship:

$$\dot{\tau}^\alpha = \sum_{\beta=1}^{n\,\mathrm{slip}} h^{\alpha\beta} \left| \dot{\gamma}^\beta \right| \tag{6}$$

where $h^{\alpha\beta}$ are slip hardening moduli, and the sum ranges over all activated slip systems. $h^{\alpha\alpha}$, and $h^{\alpha\beta}$ are self- and latent hardening moduli, respectively.

Table I. Material properties used in FE analysis

Material	Elastic modulus (GPa)	Poisson's ratio
Copper[24]	114	0.31
Solder alloy[24]	48	0.36
Cu_6Sn_5[47]	116	0.31

Material	Plastic constants: Yield strength (Mpa)	Plastic constants: Flow region
Solder alloy	21.5	Stress, $\tau = 37 \times \varepsilon^{0.075}$ where ε is the strain from 0.001 to 0.016. After this point, the solder becomes perfectly plastic[48]
Cu_6Sn_5	2700	Perfect plastic

The latent hardening modulus can be calculated from the self-hardening modulus with the inclusion of a latent hardening constant. The expression can be portrayed as:

$$h^{\alpha\beta} = q^{\alpha\beta} h^{\alpha\alpha} \tag{7}$$

where $q^{\alpha\beta}$ is the latent hardening constant which is the ratio of the latent hardening to the self-hardening rate. $q^{\alpha\beta}$ can be assumed as the following for a coplanar slip system[44]:

$$q^{\alpha\beta} = \begin{cases} 1 \text{ when } \alpha = \beta \\ q \text{ when } \alpha \neq \beta \end{cases}$$

The hyper-secant law, provided by Peirce et al.[45] has been utilized here to calculate the self-hardening moduli for the slip systems:

$$h^{\alpha\alpha} = h^0 \mathrm{sech}^2 \left| \frac{h^0 \gamma}{\tau^s - \tau^0} \right| \tag{8}$$

In this formulation, h^0 = initial hardening modulus, γ = cumulative shear strain for all slip systems, and τ^s = saturation stress.

MATERIAL PROPERTIES PARAMETERS

In this study, both conventional FE and CPFE analyses were performed for different sections. Material properties for FE analysis were consistent for all FE analyses. Similarly, CPFE parameters were kept constant for all CPFE analyses.

FE Model Parameters

To investigate the differences in conventional FE and CPFE analyses in predicting mechanical performance, the same geometrical model was used for both FE and CPFE analyses. In the regular FE model, Cu is assumed to be elastic and isotropic. The solder and Cu_6Sn_5 IMC is taken to be linearly isotropic up to the yield point. After the yield point, the solder and IMC follow the plastic behavior described in Table I. The elastic–plastic properties used in FE analysis are listed in Table I. Commercially available finite element program ABAQUS[46] was utilized for both FE and CPFE analysis.

Table II. Slip system for considered materials

Set number	Slip system	# in family
Sn (Tin)		
1	{100} ⟨001]	2
2	{110} ⟨001]	2
3	{100} ⟨010]	2
Cu_6Sn_5 IMC		
1	Basal {0001} $\langle 11\bar{2}0 \rangle$,	3
2	Prismatic $\{10\bar{1}0\}$ $\langle 11\bar{2}0 \rangle$	3
3	Pyramidal ⟨a⟩ $\{10\bar{1}1\}$ $\langle 11\bar{2}0 \rangle$	6

CPFE Model Parameters

Cu_6Sn_5 is the main IMC component that must form in any successful joint. Interestingly, this compound typically grows in a certain orientation with the *c*-axis of the hexagonal close-packed (HCP) crystal perpendicular to the copper substrate.[47] Previously, Cu_6Sn_5 elastic stiffness constants were calculated by resonant ultrasound spectroscopy (RUS), as published by Jiang et al.[48] On the other hand, CPFE plastic model parameters for Cu_6Sn_5 IMC were previously computationally generated and reported by Choudhury et al.[49] CPFE model parameters for bulk Sn were taken from the literature.[34,41] Bieler et al.[50] have reported the three most active slip systems of Sn and they have been used in this model. The three most active slip systems of HCP crystal (basal, prismatic and 1st order pyramidal)[51] were considered here as the most active slip systems of Cu_6Sn_5. The slip systems considered as CPFE model parameters are shown in Table II. A small reference shearing rate of $0.001\ s^{-1}$ was assumed in this approach as a quasi-static reference. This assumption is a

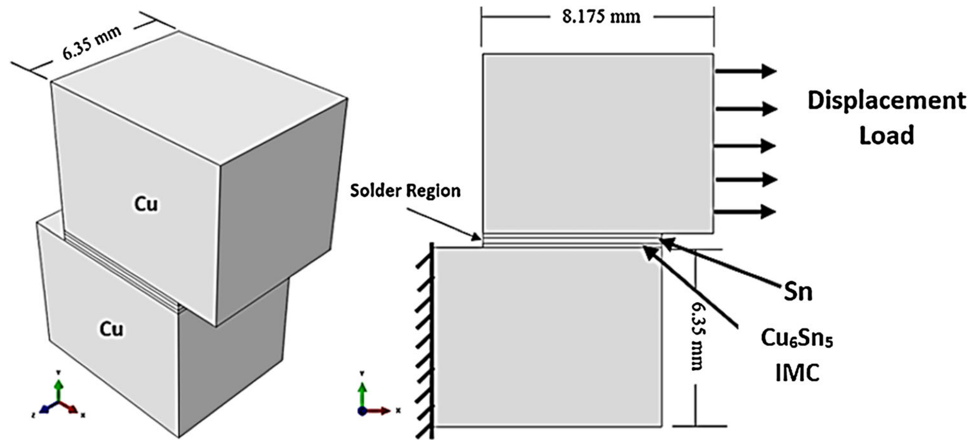

Fig. 2. Schematic model of the joint with applied boundary conditions. Dimensions are not to scale.

convenient fitting method where reference values can be taken from the quasi-static test process.[52] All other parameters are listed in the Table II. Cu is assumed to be polycrystalline and is taken as an isotropic material. Its properties are kept similar to those of the FE analysis. Commercially available FE software, ABAQUS, in combination with an extended user material subroutine, UMAT, was used for the CPFE simulations.

MODEL VALIDATION

A lap-shear joint test experiment performed by Chawla and his group[24,53] was selected to validate the CPFE model. They performed lap-shear tests on different solder joint thickness specimens, and also performed FE analysis to further analyze their results. The test was mimicked exactly to compare the FE responses with the shear test results. Two Cu substrates, with a width of 6.35 mm, length of 8.175 mm, and height of 6.35 mm, were soldered with Sn-3.5Ag solder alloy with varying joint thicknesses. The solder region was of 6.35 mm × 6.35 mm. In the experiment performed by Chawla et al., shear responses were recorded at the far field end using an extensometer and at solder joint region using a thin line created on the joint and tracking the displacements of the line. The tests were performed at ~0.001/s far field shear strain rate. The described dimensions of the joint in the study were used to create a FE model (Fig. 2). Solder joints with thickness of 520 μm and 120 μm were selected in this numerical experiment. Both models, 520 μm and 120 μm, had the same shear strain which was achieved by applying different displacement loads for the same time. Element type C3D8R was used to generate the FE mesh, where a stress-based mesh sensitivity analysis was performed to achieve an optimum model.

Solder, and Cu_6Sn_5 IMC were considered as a single crystal in the CPFE analysis for simplification without considering variation in crystallographic orientation in this validation model. The

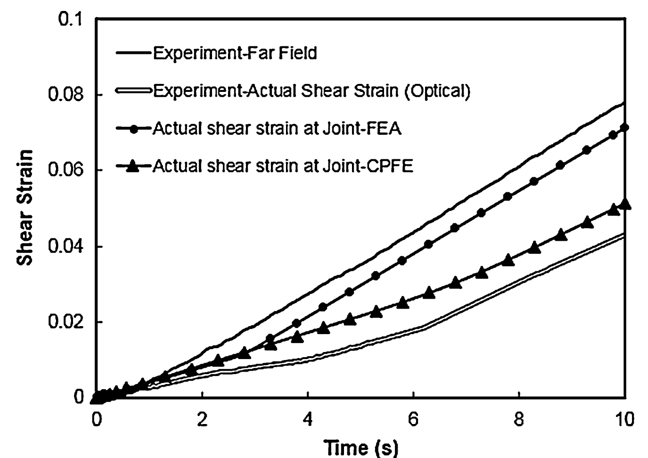

Fig. 3. Shear strain versus time for the 120-μm solder joint. Data for experimental far field and actual shear strain measured optically are from.[24]

c-axis of Sn was considered to be oriented along the shear loading axis. Previously, it was observed that Cu_6Sn_5 grows along the c-axis which is normal to the solder/Cu surface.[47] A similar orientation was considered for Cu_6Sn_5 where the c-axis was oriented normal to the solder/Cu surface. Due to the large scale of the model, inclusion of IMC roughness in the model would introduce complexity. So, for simplification and computational time, the roughness of IMC morphology was not taken into consideration. CPFE analysis were performed with 20% IMC and without IMC to capture the effect of IMCs on the shear behavior of the solder joint.

Validation Results

Figure 3 shows a plot of shear strain versus time. The far field shear strain is almost linear with time, as prescribed by the applied shear strain rate. However, in the experiment, a lower nonlinear shear strain was observed at the solder region. The divergence is due to the deformation associated with Cu and the fixture, etc. In FE

Table III. Stiffness matrix for considered materials

Stiffness matrix (MPa)
Cu_6Sn_5 IMC[48]
C_{11} = 96500, C_{22} = 96500, C_{33} = 96500, C_{44} = 32100, C_{55} = 32100, C_{66} = 32100, C_{12} = 32400, C_{13} = 32400, C_{23} = 32400
Sn (Tin)[34]
C_{11} = 72300, C_{22} = 72300, C_{33} = 88400, C_{44} = 22000, C_{55} = 22000, C_{66} = 24000, C_{12} = 59400, C_{13} = 35800, C_{23} = 35800

Table IV. CPFE model parameters

	τ_{crss} (MPa)	τ_s (MPa)	h^0 (MPa)	n	q
Sn (Tin)[35]	23	40	100 [set 1,2] 150 [set 3]	10	1.4
Cu_6Sn_5[49]	260 [set 1] 1500 [set 2] 1310 [set 3]	$2.5\tau_{crss}$	12,000	12.2	1
Cu[41]	60.8	109.5	541.5	10	1

models, to measure the actual shear strain at the joint area, the displacements at the nodes in the solder region area were taken into consideration and then averaged to get the average shear strain. CPFE results show slightly higher values compared to the actual shear strain measured optically *in situ*, although the shear strain accumulation rate was similar in both experiments and CPFE analysis. Initially, the slow buildup of shear strain is seen where the solder behaves elastically. After a time, the solder starts to deform plastically and the shear strain rate becomes higher. The smaller discrepancies between the experimental and CPFE models may have been caused by several factors such as consideration of single crystal for both solder, variation in input parameters, etc. The Cu substrate dimension was large enough to have many grains so that it behaves as isotropic bulk material. To keep consistency with other analyses performed later in this study, all materials were modeled with the CPFE material parameters presented in Tables II, III, and IV.

Results extracted from traditional FE analysis followed the far field shear strain response more closely. As FE analysis is unable to capture the intrinsic material deformation mechanism, the shear strain response with respect to time was not able to predict the actual local shear strain behavior which was measured optically in the experiment.

To compare the shear stress–strain response in experimental findings and finite element analysis, the shear stress versus far field shear strain was plotted. Shear stress was calculated by dividing the applied load by the solder pad area. Figure 4 shows the shear stress–strain response for the 120-μm thickness joint. The simulation results in a slightly different slope in the elastic region compared to the experimental result. The predicted yield strength during the CPFE model shows similar values compared to the experimental results. However, when 20% IMC was included in the model, the result showed a stiffer response. This phenomenon is due to the different mechanical properties of the Cu_6Sn_5 IMC which has a relatively stiffer elastic response with higher yield strength. Analysis shows that overall hardening behavior of the joint increases with the inclusion of IMC in the model. However, the CPFE model was able to successfully predict the qualitative elastic–plastic behavior of the solder joint.

Traditional FE analysis shows lower yield strength values than the apparent experimental yield strength values. This is due to the differences in intrinsic material behavior of small sized solder than bulk solder input properties.

Similar analysis has been conducted for the 520-μm thickness joint, and Fig. 5 contains the shear stress-shear strain response. The effect of 20% Cu_6Sn_5 IMC inclusion shows higher changes in apparent stiffness compared to the effect on 120 μm thickness joint. Chawla et al. did not provide any information regarding the IMC thickness in the solder joint. However, model with 20% IMC shows almost identical experimental response. Traditional FE provides less yield strength compared to experiment.

An important finding of Chawla et al.[53] was the shear behavior of solder joints with different joint thicknesses. With the increasing solder joint thickness, the joint shows higher apparent stiffness. It was concluded by Chawla et al. that, at lower thickness, the deformation was transmitted through both normal and shear components. With the increase in joint thickness, the shear component becomes more dominant and provides a stiffer shear response. To investigate this finding, the shear

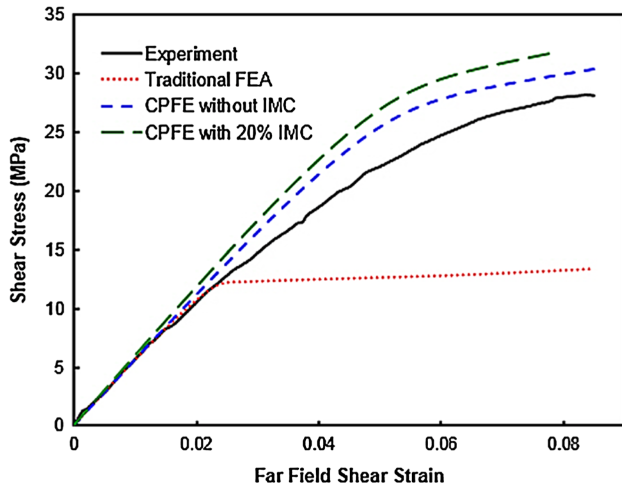

Fig. 4. Shear stress versus far field shear strain for the 120-μm solder joint. Figure contains the shear response extracted during traditional FEA, CPFE modeling with and without IMC, and experimental finding. Experimental data are reproduced from Ref. 24.

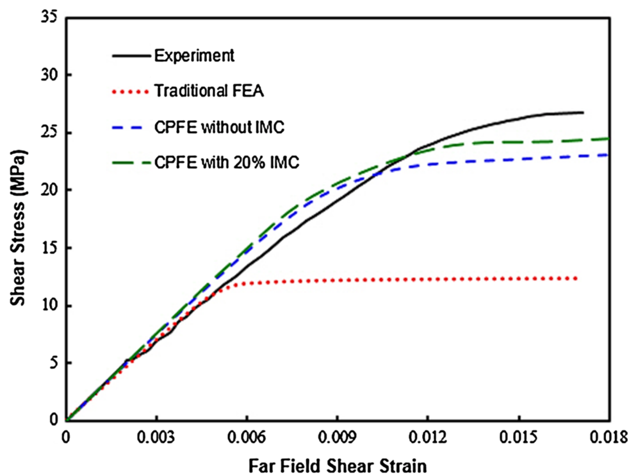

Fig. 5. Shear stress vs. far field shear strain for the 520-μm solder joint. The figure contains the shear response extracted during traditional FE and CPFE modeling with and without IMC, and the experimental finding. Experimental data are reproduced from Ref. 24.

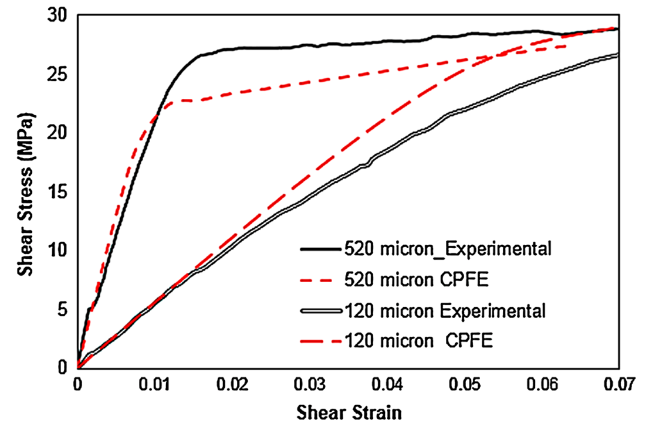

Fig. 6. Comparison of shear stress–strain responses for 520 μm and 120 μm solder joints. CPFE model contains no IMC here for simplification. Experimental data are reproduced from Ref. 24.

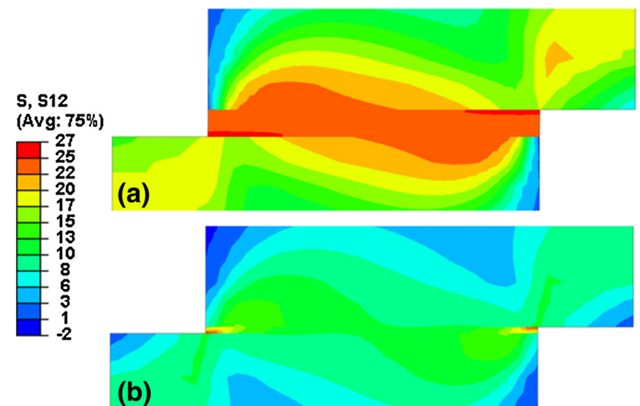

Fig. 7. In-plane shear stress (in MPa) contour plot for (a) 520 μm and (b) 120 μm solder joints, at a shear strain of 0.020. The contour plots are showing a portion of Cu substrate to focus largely on the joint.

stress–strain response in CPFE analysis for both the 120-μm and 520-μm thickness joints are plotted in Fig. 6. As seen in this figure, CPFE shows a similar trend. The thicker solder joint provided a stiffer shear response whereas the thin joint showed less stiff performance. Figure 7 shows the in-plane shear stress contour plot for these joint thickness at a 0.020 far field shear strain. It is evident in CPFE analysis that the thicker solder joint shows higher shear stress at the solder area. On the other hand, the in-plane shear stress at thin solder joint is almost continuously distributed with only a little higher in-plane shear stress at the corner. The thinner solder joint behaves as a Cu–solder–Cu assembly where the shear stress is distributed in the whole assembly. In-plane shear strain is large at the solder region at the thicker solder joint, indicating that large deformation occurs at the solder region for the thicker solder joint. A relatively distributed in-plane logarithmic shear strain is found for the thinner solder joint indicating mechanical load diffused through the greatly constrained joint without inducing large shear strain in the solder region. The findings in this model are supported by the numerical results published by Shen et al.,[53] and Chawla et al.[24] The model was able to capture the geometric effect where the thicker joint showed a higher stiffness and the thinner joint showed a lower stiffness.

EFFECT OF IMC THICKNESS THROUGH CPFE

Model Generation

A simple shear specimen were selected to conduct the CPFE analysis. A square block of 100 μm $\times$ 100 μm $\times$ 100 μm of solder material was

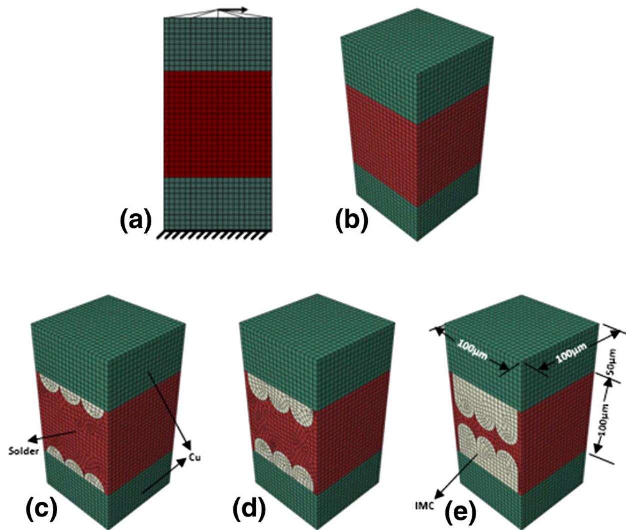

Fig. 8. Meshed model showing (a) boundary conditions, and models with different IMC thicknesses such as (b) no IMC, (c) 20 μm IMC, (d) 40 μm IMC, and (e) 80 μm IMC.

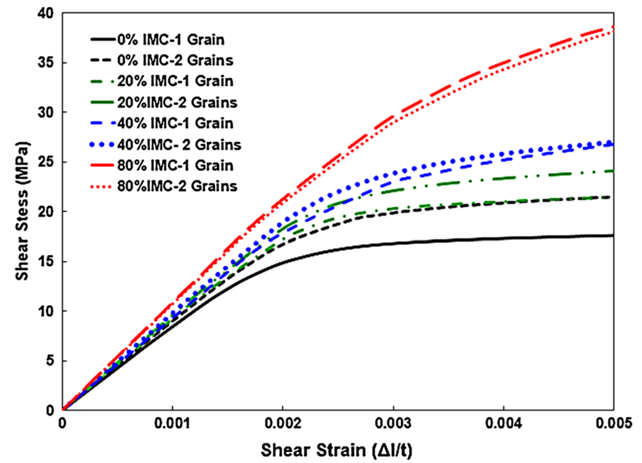

Fig. 9. The effect of IMC thickness on the shear stress–shear strain behavior of a single crystal Sn solder joint and a bicrystal Sn solder joint.

sandwiched by two blocks of Cu material of 100 μm $\times$ 100 μm $\times$ 50 μm (Fig. 8). The upper and lower blocks of 100 μm $\times$ 100 μm $\times$ 50 μm were assigned Cu material properties for CPFE analysis. Solder material properties were allocated to the middle block, which was considered as one crystal for single crystal Sn analysis. To investigate the bicrystal Sn, the middle block was divided into half and a different crystallographic orientation was assigned to the two parts. Generally, Cu_6Sn_5 IMC exhibits a scallop-type microstructure. To take IMC into consideration and to simplify the model, Cu_6Sn_5 IMC was modeled as three half-cylinders. These half-cylinders were grown on the solder/Cu interface to change the thickness of IMC. Three different IMC thicknesses of 20 μm, 40 μm, and 80 μm were considered to analyze the effect of IMC thickness on the shear behavior of the solder joint.

The bottom surface of the model was fixed in all directions while the displacement load was assigned to the top surface to introduce the shear behavior (Fig. 8a). The same displacement load was assigned for all models to have a similar shear strain rate so that comparative analysis could be conducted. The whole assembly was meshed with the C3D8R element, and stress-based mesh sensitivity analysis were performed to find the optimum mesh size.

Shear stresses for all analyses were calculated by dividing the applied load by the solder pad area which was 0.01 m^2. Shear strain was obtained by the conventional relationship- of displacement divided by joint thickness.

Model Results for Single Crystal Sn

For this analysis, single crystal Sn with its *c*-axis oriented towards the loading direction is considered, as it is statistically the most common crystallographic orientation observed for single grain Sn in solder joints.[54,55] Generally, the Sn crystal tends to grow along the $\langle 110]$ direction which is the preferred grain growth direction.[56] When the heat flows from substrate to substrate during the reflow process, the $\langle 110]$ direction follows the heat flow direction which is perpendicular to the substrate. This phenomenon aligns the *c*-axis [001] parallel to the substrate normal which happens to be situated 90° to the $\langle 110]$ direction.[55] Cu_6Sn_5 IMC thicknesses were varied between 20 μm, 40 μm and 80 μm (Fig. 8). Shear stress–strain is plotted in Fig. 9. It has been observed that, with the increase in IMC thickness, the solder joint provides a stiffer response and higher shear yield strength. Cu_6Sn_5 has a much higher yield strength than Sn. Larger volume ratios of Cu_6Sn_5 will have a dominant effect on shear yield strength and will increase the overall shear yield strength of the joint. The rigid nature of Cu_6Sn_5 induces larger constraints on the joint and tends to introduce rigid body behavior. Apparently, the increase in stiffer material in the solder joint causes the shear stress–strain behavior to change from 'low stiffness–low strain hardening' to 'high stiffness–high strain hardening'. Similar effects of IMC thickness on the experimental shear response have been reported previously[17,57] although their effects were not significant as their specimens were larger. Effects of IMC thickness on the mechanical behavior would be more dominant when the size of the joint becomes smaller. Recently, Choudhury et al.[58] performed single lap-shear tests on different IMC thickness joints and observed similar behavior where higher IMC thickness contributed to stiffer responses.

An in-plane shear stress contour plot is provided in Fig. 10 for 4 models with different IMC thicknesses at a 0.02 shear strain. It can be seen that models with IMCs develop higher in-plane shear

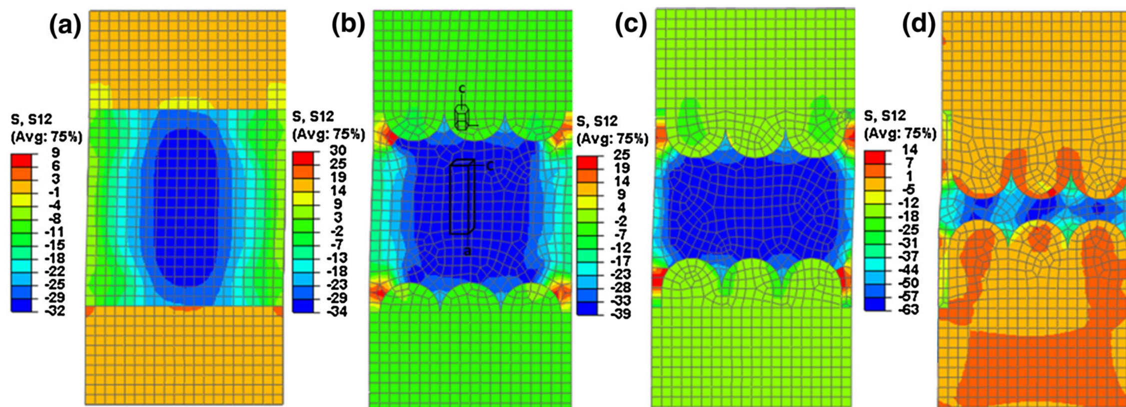

Fig. 10. In-plane shear stress contour plot for IMC thickness of (a) no IMC, (b) 20 μm, (c) 40 μm, and (d) 80 μm in a single crystal solder joint model at 0.02 shear strain. The orientation of the crystals are given.

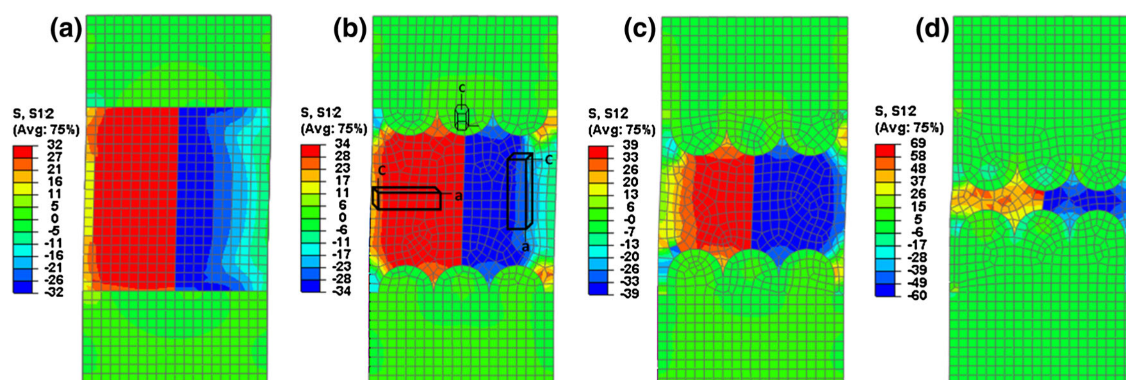

Fig. 11. In-plane shear stress contour plot for IMC thickness of (a) no IMC, (b) 20 μm, (c) 40 μm, and (d) 80 μm in bicrystal solder joint model at 0.02 shear strain. The orientation of the crystals are given.

stress in the solder/Cu_6Sn_5 IMC interface. This could result in crack initiation and growth at the solder/Cu_6Sn_5 IMC interface. Failure in solder/IMC interface has been observed by several researchers.[19,59,60] On the other hand, accumulation of in-plane shear stress in the Sn region increases with the increase in IMC thickness. At the same shear strain, the magnitude of shear stress at the 80-μm IMC thickness joint is 2 times higher than the 20-μm IMC thickness joint.

Model Results for Bicrystal Sn

Two orientations were selected to simulate bicrystal Sn in the joint. The orientation is shown in Fig. 11. The shear stress–shear strain responses were recorded and are shown in Fig. 9. It has been observed that the bicrystal Sn model without Cu_6Sn_5 IMC shows noticeable differences compared to single crystal Sn. However, as the Cu_6Sn_5 IMC thickness increases, the effect seems to diminish and the shear behavior becomes similar to single crystal (Fig. 9). Due to the geometric effect discussed earlier, a stiffer response was observed for the higher Cu_6Sn_5 IMC thickness joint. At higher Cu_6Sn_5 IMC thickness, the solder joint exhibitsa stiffer response with higher shear yield strength. The hardening behavior of the solder joint becomes dominated by Cu_6Sn_5 behavior where the plastic shear deformation is achieved at higher shear stresses.

Small regions of stress concentrations were found on the hills of the IMCs. Other than that, no continuous higher stress concentrations were observed in the solder joint. Overall response for the solder joint was similar to the single crystal solder joint.

DISCUSSION

Sn has a body-centered tetragonal crystal structure where the *c*-axis to *a*-axis lattice parameter ratio, *c*/*a*, is 0.5456.[26] The large discrepancy in the lattice parameter and the large grain microstructure observed in solder alloys introduces anisotropy. The elastic modulus and the co-efficient of thermal

expansion (CTE) are reported to vary greatly with the crystallographic direction.[35,61] To understand the effect of Sn anisotropy on the modeled solder joint, two analyses were conducted on a single crystal Sn with the loading direction keeping along the *c*-axis and along the *a*-axis. A simple cubic block was designed and Sn crystal plasticity parameters were assigned to it. The crystallographic orientation was changed with respect to the shear loading direction. The shear stress–strain response shows a noticeable anisotropic effect (Fig. 12). The joint provides overall lower shear yield strength when the loading direction was along the *c*-axis. An almost 40% increase in shear yield strength was observed when the crystal was rotated and the *a*-axis was aligned along with the loading direction. Similar behavior was reported by Darbandi et al.[34] from their shear test simulation. Shear yield strength was lowest in their study when the crystal was oriented in such a way that the *c*-axis was parallel to the loading direction. The phenomenon is understood when we look into the average shear strain in most active slip systems in Sn (Fig. 13). The shear strains in the slip systems were averaged from the elements in Sn area. When the *a*-axis of Sn is aligned along the loading direction, (100) [010] is the most active slip system, and other slip systems do not contribute significantly. Thus, the crystal shows higher stiffness and higher yield strength. On the other hand, in the case of the *c*-axis of the crystal oriented along the loading direction, multiple slip systems contribute towards the deformation, providing easy deformation. In this case, (100) [001] is the most active slip system, and the (110) [001] slip system also contributes noticeably.

The effect of the increase in IMC thickness was clearly observed when the elastic regime of the shear stress–strain curve and shear yield strengths were compared (Fig. 9). It is evident that solder joints show a stiffer elastic response when the fraction of IMC increases. If we compare the individual elastic stiffness matrices of both Sn and Cu_6Sn_5 given in Table III, we can see that the Cu_6Sn_5 IMC has higher stiffness than Sn. Thus, due to the increase in Cu_6Sn_5 thickness, the overall solder joint shear behavior tends to show a stiffer response. On the other hand, when the joint has a larger volume of Cu_6Sn_5 IMC, shear deformation becomes tougher due to the higher slip yielding properties of Cu_6Sn_5 IMC, resulting in overall higher shear yield strength. It can also be observed from Fig. 9 that, when the model had low IMC thickness, the differences in shear response between the single and bicrystal models can be clearly seen. However, with the increase in IMC thickness, the differences start to diminish. The model with 80 μm IMC has an almost identical shear response for the single crystal and bicrystal models. However, due to the absence of any failure criteria, the plastic regime of the shear stress–strain curve may not be practical. It has been observed in the literature that, due to the hardness and brittleness of the IMCs, joints with higher volume fractions of IMCs tend to fail at a smaller strain while joints with thin IMCs provide larger strains to failure.[58]

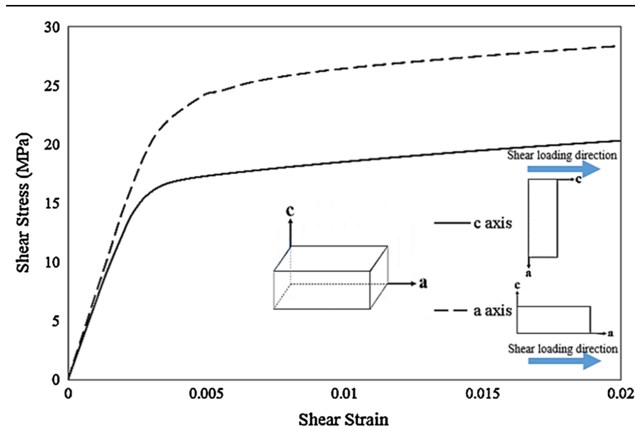

Fig. 12. Shear stress–strain response for a solder joint with different orientations of Sn. The orientation schematic is provided in the inset.

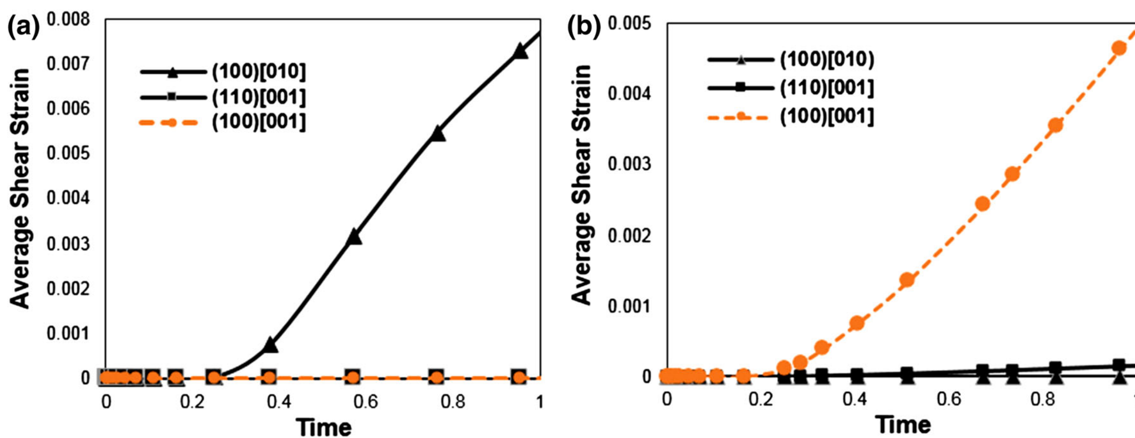

Fig. 13. Evaluation of average shear strain in slip systems of Sn in the solder joint, when (a) the *a*-axis oriented along the loading direction, (b) the *c*-axis is oriented along the loading direction.

CONCLUSIONS

Interconnect materials have an anisotropic effect due to their crystal structure. This anisotropy has significant effects on the mechanical properties of micro-solder joints. The findings observed during this study are:

- It has been shown that CPFE models perform better than traditional FE models to predict the mechanical behavior in small-scale solder joints. CPFE models use the crystal slip deformation information to predict how materials with few grains behave mechanically. On the other hand, traditional FE models take bulk material properties into account which leads to inaccurate predictions of plastic behavior or insufficient results of material behavior at the micro-scale. A single lap shear test was selected to validate the CPFE model. The model was able to predict the elastic–plastic material behavior of the overall solder joint.
- The effect of IMC thickness on the shear deformation of the solder joint was also analyzed for solder joints with single and bicrystal Sn. With the increase in IMC thickness, the solder joint gives a stiffer shear response while increasing the shear yield strength. When the solder joint has la arger volume of Cu_6Sn_5 IMC, shear deformation becomes harder due to the higher yielding properties of Cu_6Sn_5 IMCs, thus giving overall higher shear yield strength.

Crystal plasticity finite element models can accurately predict the qualitative behavior of the material. The model can be utilized as a suitable tool to predict the mechanical behavior of solder joints and may contribute towards developing solder interconnects with higher reliability.

ACKNOWLEDGEMENTS

This paper is based upon work supported by the National Science Foundation (NSF) under The Division of Civil, Mechanical and Manufacturing Innovation (CMMI) Grant No. 1416682. The authors greatly appreciate the support from NSF.

REFERENCES

1. I. Panchenko, K. Croes, I. De Wolf, J. De Messemaeker, E. Beyne, and K.-J. Wolter, *Microelectron. Eng.* 117, 26 (2014).
2. O.M. Abdelhadi and L. Ladani, *J. Electron. Packag.* 135, 021004 (2013).
3. P. Protsenko, A. Terlain, V. Traskine, and N. Eustathopoulos, *Scr. Mater.* 45, 1439 (2001).
4. D.R. Frear, *JOM* 48, 49 (1996).
5. R.E. Pratt, E.I. Stromswold, and D.J. Quesnel, *J. Electron. Mater.* 23, 375 (1994).
6. Y. Chan, A.C. So, and J.K. Lai, *Mater. Sci. Eng. B* 55, 5 (1998).
7. I. Panchenko, J. Grafe, M. Mueller, and K.-J. Wolter, in *2013 IEEE 15th Electron. Packag. Technol. Conf.* (2013), pp. 318–323.
8. B.L. Chen and G.Y. Li, *Thin Solid Films* 462–463, 395 (2004).
9. P. Liu, P. Yao, and J. Liu, *J. Alloys Compd.* 470, 188 (2009).
10. M. Sona and K.N. Prabhu, *J. Mater. Sci.* 25, 1446 (2014).
11. J. Amistoso and A.V. Amorsolo, *IEEE Trans. Compon. Packag. Technol.* 32, 405 (2009).
12. X. Hu, Y. Li, Y.Y. Liu, Y.Y. Liu, and Z. Min, *Microelectron. Reliab.* 54, 1575 (2014).
13. O.M. Abdelhadi and L. Ladani, *J. Alloys Compd.* 537, 87 (2012).
14. L. Yang and Z.F. Zhang, *J. Electron. Mater.* 44, 590 (2014).
15. T. An and F. Qin, *Microelectron. Reliab.* 54, 932 (2014).
16. H.-T. Lee, M.-H. Chen, H.-M. Jao, and T.-L. Liao, *Mater. Sci. Eng. A* 358, 134 (2003).
17. X. Deng, R.S. Sidhu, P. Johnson, and N. Chawla, *Metall. Mater. Trans. A* 36, 55 (2005).
18. Y.J. Chen, C.K. Chung, C.R. Yang, and C.R. Kao, *Microelectron. Reliab.* 53, 47 (2013).
19. C. Chen, L. Zhang, J. Zhao, L. Cao, and J.K. Shang, *J. Electron. Mater.* 41, 2487 (2012).
20. Y.-H. Lee and H.-T. Lee, *Mater. Sci. Eng. A* 444, 75 (2007).
21. K.N. Bhat, K.N. Prabhu, and Satyanarayan, *J. Mater. Sci.* 25, 864 (2014).
22. S.-T. Lu, J.-Y. Juang, H.-C. Cheng, Y.-M. Tsai, T.-H. Chen, W.-H. Chen, and S. Lu, et al., *IEEE Trans. Device Mater. Reliab.* 12, 296 (2012).
23. Y. Liu, F. Sun, L. Luo, C.A. Yuan, and G. Zhang, *J. Electron. Mater.* 44, 2450 (2015).
24. N. Chawla, Y.-L. Shen, X. Deng, and E.S. Ege, *J. Electron. Mater.* 33, 1589 (2004).
25. F. Ochoa, X. Deng, and N. Chawla, *J. Electron. Mater.* 33, 1596 (2004).
26. T.R. Bieler, H. Jiang, L.P. Lehman, T. Kirkpatrick, and E.J. Cotts, in *2006 IEEE 56th Electron. Components Technol. Conf.* (2006), pp. 1462–1467.
27. B. Zhou, Q. Zhou, T.R. Bieler, and T. Lee, *J. Electron. Mater.* 44, 895 (2015).
28. J. Rayne and B.S. Chandrasekhar, *Phys. Rev.* 120, 1658 (1960).
29. D.G. House and E.V. Vernon, *Br. J. Appl. Phys.* 11, 254 (1960).
30. L. Jiang, H. Jiang, and N. Chawla, *J. Electron. Mater.* 41, 2083 (2012).
31. M.A. Matin, E.W.C. Coenen, W.P. Vellinga, and M.G.D. Geers, *Scr. Mater.* 53, 927 (2005).
32. S. Park, R. Dhakal, and J. Gao, *J. Electron. Mater.* 37, 1139 (2008).
33. J. Gong, *Comput. Mater. Sci.* 43, 199 (2008).
34. P. Darbandi, T.R. Bieler, F. Pourboghrat, and T. Lee, *J. Electron. Mater.* 42, 201 (2013).
35. P. Darbandi, T. Lee, T.R. Bieler, and F. Pourboghrat, *Comput. Mater. Sci.* 85, 236 (2014).
36. M. Maleki, J. Cugnoni, and J. Botsis, *Acta Mater.* 61, 103 (2013).
37. R.J. Asaro and A. Needleman, *Acta Metall.* 33, 923 (1985).
38. E.W. Schmid and W. Boas, *Plasticity of Crystals* (London: F. A. Hughes & Co. Ltd, 1950), pp. 200–313.
39. R. Hill and J.R. Rice, *J. Mech. Phys. Solids* 20, 401 (1972).
40. J.R. Rice, *J. Mech. Phys. Solids* 19, 433 (1971).
41. Y. Huang, *Mech. Report* (Cambridge: Harvard University, 1991).
42. E.H. Lee, *J. Appl. Mech.* 36, 1 (1969).
43. J. Pan and J.R. Rice, *Int. J. Solids Struct.* 19, 973 (1983).
44. U.F. Kocks, *Metall. Mater. Trans.* 1, 1121 (1970).
45. D. Peirce, R.J. Asaro, and A. Needleman, *Acta Metall.* 30, 1087 (1982).
46. D. Hibbitt, B. Karlsson, and P. Sorensen, *Abaqus/CAE User's Guide, ABAQUS 6.11* (Providence, RI: Dassault Systèmes Simulia Corp., 2013).
47. S.F. Choudhury and L. Ladani, *J. Electron. Mater.* 43, 996 (2014).
48. L. Jiang, N. Muthegowda, M.A. Bhatia, A. Migliori, K.N. Solanki, and N. Chawla, *Scr. Mater.* 107, 26 (2015).
49. S.F. Choudhury and L. Ladani, *Metall. Mater. Trans. A* 46, 1108 (2014).
50. T.R. Bieler and A.U. Telang, *J. Electron. Mater.* 38, 2694 (2009).
51. M.H. Yoo, *Metall. Trans. A* 12, 409 (1981).

52. F. Roters, P. Eisenlohr, L. Hantcherli, D.D. Tjahjanto, T.R. Bieler, and D. Raabe, *Acta Mater.* 58, 1152 (2010).
53. Y.-L. Shen, N. Chawla, E.S. Ege, and X. Deng, *Acta Mater.* 53, 2633 (2005).
54. H. Chen, B. Yan, M. Yang, X. Ma, and M. Li, *Mater. Charact.* 85, 64 (2013).
55. P. Liu, A. Overson, and D. Goyal, in *2015 IEEE 65th Electron. Components Technol. Conf.* (2015), pp. 99–105.
56. B. Arfaei, N. Kim, and E.J. Cotts, *J. Electron. Mater.* 41, 362 (2012).
57. H.-T. Lee, S.-Y. Hu, T.-F. Hong, and Y.-F. Chen, *J. Electron. Mater.* 37, 867 (2008).
58. S.F. Choudhury and L. Ladani, *J. Alloy Compd.* (2016). doi:10.1016/j.jallcom.2016.04.184.
59. F. Song and S.W.R. Lee, in *2006 IEEE 56th Electron. Components Technol. Conf.* (2006), pp. 1196–1203.
60. J.-M. Kim, M.-H. Jeong, S. Yoo, C.-W. Lee, and Y.-B. Park, *Microelectron. Eng.* 89, 55 (2012).
61. A. Zamiri, T.R. Bieler, and F. Pourboghrat, *J. Electron. Mater.* 38, 231 (2009).